New Journal of Physics
The open access journal at the forefront of physics
Deutsche Physikalische Gesellschaft DPG IOP Institute of Physics

PAPER • OPEN ACCESS

# Enhancing directivity of terahertz photoconductive antennas using spoof surface plasmon structure

To cite this article: Chi Wang *et al* 2022 *New J. Phys.* **24** 073046

New Journal of Physics
The open access journal at the forefront of physics

Deutsche Physikalische Gesellschaft DPG
IOP Institute of Physics
Published in partnership with: Deutsche Physikalische Gesellschaft and the Institute of Physics

CrossMark

OPEN ACCESS

RECEIVED
10 March 2022

REVISED
9 July 2022

ACCEPTED FOR PUBLICATION
14 July 2022

PUBLISHED
10 August 2022



PAPER

# Enhancing directivity of terahertz photoconductive antennas using spoof surface plasmon structure

Chi Wang[1,2], Zijian Zhang[1,2], Youfei Zhang[1], Xinrong Xie[1,2], Yumeng Yang[1,2], Jiaguang Han[3], Erping Li[1], Hongsheng Chen[1,2], Jianqiang Gu[3], Wei E I Sha[1,*] and Fei Gao[1,2,*]

[1] Interdisciplinary Center for Quantum Information, State Key Laboratory of Modern Optical Instrumentation, College of Information Science and Electronic Engineering, Zhejiang University, Hangzhou 310027, People's Republic of China
[2] International Joint Innovation Center, Zhejiang University, Haining 314400, People's Republic of China
[3] Center for Terahertz Waves and College of Precision Instrument and Optoelectronics Engineering, Tianjin University, Tianjin 300072, People's Republic of China
[*] Authors to whom any correspondence should be addressed.

**E-mail:** weisha@zju.edu.cn and gaofeizju@zju.edu.cn

**Keywords:** metamaterials, spoof surface plasmons, terahertz

Supplementary material for this article is available online

## Abstract

Terahertz photoconductive antenna (PCA) is an important device for generating ultrabroadband terahertz radiations, being applicable in various scenarios. However, the metallic electrodes in PCAs, a pair of coplanar strip lines (CSL), always produce horizontal electrode modes in a broad THz band, thus resulting in low directivity in the vertical direction. Here, we introduce spoof surface plasmon polariton (SSPP) structures to suppress horizontal electrode modes in a broad band. The suppression principles are accounted to both the forbidden band of the fundamental SSPP mode and the orthogonality between source and higher-order SSPP modes. In the SSPP-modified PCA, we achieve around 2 dBi higher directivity in the vertical direction compared to a typical CSL PCA. Unlike the narrow bands inheriting from conventional metamaterial resonators, the relative operational band of the SSPP-modified PCA is as broad as 48%. This planar SSPP structure is compatible with the well-developed micro fabrication technologies. Thus, our scheme can be combined with the semiconductor material engineering and plasmonic nanoscale structures for further increasing THz output power.

## 1. Introduction

Terahertz photoconductive antenna (PCA) [1, 2] is an important device for generating ultrabroadband THz radiations, which show important applications in next-generation wireless communications [3, 4], non-ionized imaging [5], non-destructive detections [6], and spectroscopic analysis [7, 8]. The general principle of PCAs is that the picosecond carriers excited by femtosecond laser are driven by the biased voltages to generate THz radiations. Figure 1(a) is a typical PCA, whose horizontal and vertical directions are along $x$- and $z$-axis respectively. The vertical radiation of the PCA is usually harnessed for various applications. However, applications of THz PCAs are hindered by their low output efficiencies. The low-output issue originates from two reasons, including the low optical-to-THz conversion efficiency and low vertical directivity induced by horizontal electrode modes in PCAs.

Until now, much effort has been devoted to increasing the output efficiencies of PCAs. To address the output issues, nanoscale structures [9–22], the choice of semiconductor photoconductive materials via strain-coupled heterostructures [23–25] and using the Ge/Rh-doped substrates [26], have been introduced into PCAs. However, these schemes only increase optical-to-THz conversion efficiency, but are incapable to eliminate electrode modes in PCAs. Especially, the metallic electrodes, a pair of coplanar strip lines (CSL), always lead to transmission-line (TL) electrode modes in a broad THz band. The horizonal modes further

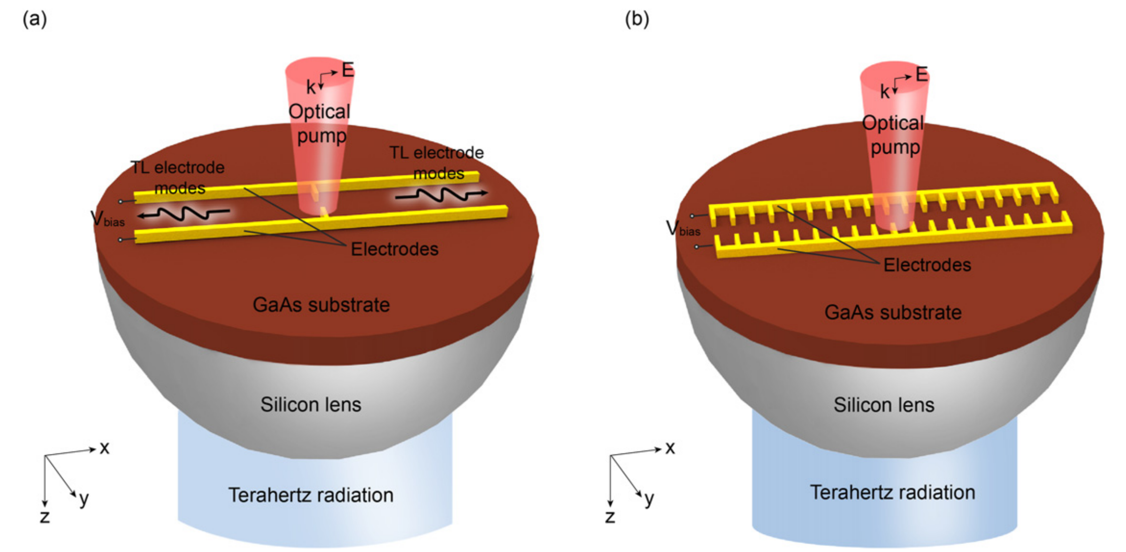


**Figure 1.** Schematic of a terahertz SSPP-modified PCA. (a) A typical CSL PCA, and (b) a SSPP-modified PCA.

result in the reduction of vertical directivity of THz PCAs. Integrating microscale metamaterial resonators with PCAs provide feasible routes to suppress the TL electrode modes at specific frequencies, thus increasing directivities of PCAs in narrow bands [27–32].

Here, we propose a scheme to increase the directivity of PCAs in a broad band, by incorporating spoof surface plasmon polariton (SSPP) [33–35] structures in PCAs. The SSPP structure is a subwavelength metallic grating, which can host surface electromagnetic (EM) modes, analogous to surface plasmon polariton (SPP) in nano optics [36–38]. Different from the circuit-modeling scheme [39] improving output powers at specific frequencies, the SSPP-modified electrode can enhance directivity of the PCA antenna in a band of relative width 48%, and simultaneously achieve around 2 dBi higher directivity in the vertical direction than that of a typical CSL. This design allows for applying THz PCAs to sensing, imaging, and detections.

## 2. Results

Figure 1 shows the schematic diagrams of a typical CSL and a SSPP-modified PCAs. The typical PCA in figure 1(a) shows a CSL gold structure patterned on a gallium arsenide (GaAs) substrate. The terahertz radiation is generated at the center of the CSL structure, and collimated along the vertical ($+z$) direction by a silicon lens. However, partial THz waves could be guided along the CSL and form TL modes, which can travel horizontally, thus reducing the THz emission along the vertical ($+z$) direction. To address the issue of horizontal electrode modes, we propose a SSPP-modified electrode as shown in figure 1(b). The SSPP structure is composed of periodic metallic grooves, which has been intensively utilized to guide surface EM waves [33].

To further quantify the advantages of the SSPP-modified electrode, we firstly compared the radiations from both CSL and SSPP-modified antennas without substrate. Both structures are illustrated in figure 2(a). They share the same parallel metallic CSL with a set of typical parameters, as length $l = 2115$ $\mu$m, width $w = 10$ $\mu$m, and separated by distance $a = 90$ $\mu$m. The parallel metallic strips in SSPP PCA are decorated by periodic metallic patches with period $p = 105$ $\mu$m, width $b = 15$ $\mu$m, and gap $g = 15$ $\mu$m. The thickness along the $z$-direction of the patches is 0.2 $\mu$m. We numerically explore the radiation performances by utilizing time-domain solver of CST Microwave Studio. In simulations, dipole sources in THz range are connected to the two metallic patches at the center of the CSL, to represent the photogenerated currents in PCAs. The boundary condition is open (add space). We employ directivity [40] $D = \max(P_{(\theta,\phi)})/P_{\text{avg}}$ to characterize the performance of PCAs, where $P_{(\theta,\phi)}$ and $P_{\text{avg}} = \frac{\int_{\theta=0}^{\pi}\int_{\phi=0}^{2\pi} P(\theta,\phi)\sin\,\theta\,\mathrm{d}\theta\,\mathrm{d}\phi}{4\pi}$ represent the radiation power in unit solid angle and average radiation power respectively. Since the CSL are along the horizonal ($x$) directions (as shown in figure 2(a)), their traveling TL modes result in the horizontal leakage with power $P_{+x}$. By simulation, we find that the SSPP-modified antenna shows lower $P_{+x}/P_{\text{avg}}$ than that of the CSL one in 0.93–1.5 THz. The radiation patterns at 0.9 and 1.1 THz (shown in figure 2(c)) further verify that the SSPP electrode can suppress the horizontal leakage, which exist in CSL ones. Simultaneously,

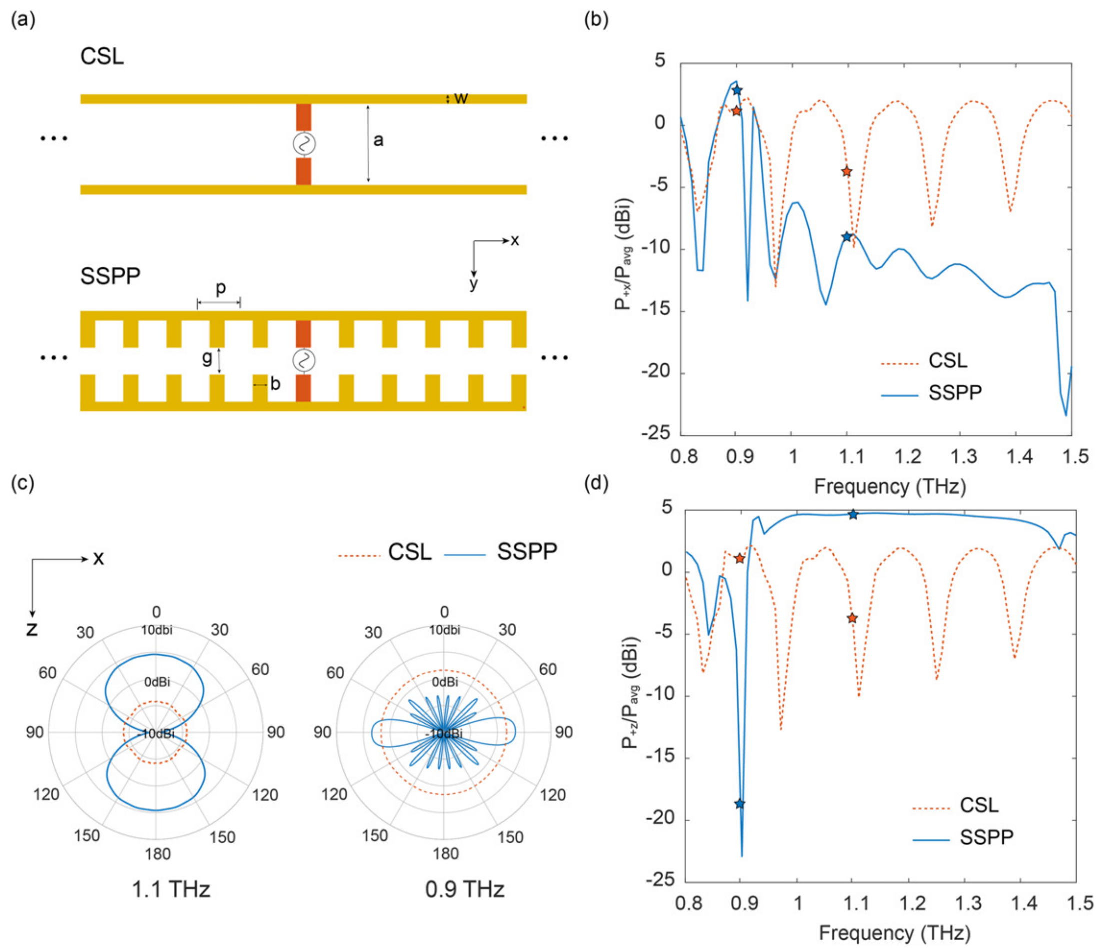


**Figure 2.** The comparison between a freestanding CSL and SSPP-modified antenna. (a) The structures of a typical CSL antenna and a SSPP-modified antenna. Both PCAs share the same parallel metallic strips with width $w = 10\ \mu$m, separated by distance $a = 90\ \mu$m. In the SSPP-modified PCA, parallel metallic strips are decorated with periodic metallic patches with period $p = 105\ \mu$m, width $b = 15\ \mu$m, and gap $g = 15\ \mu$m. (b) The $P_{+x}/P_{\text{avg}}$ of both antennas. (c) The radiation patterns in the $x$–$z$ plane of both antennas at 0.9 THz and 1.1 THz, respectively. (d) The directivities of both antennas. The dashed and solid lines represent results of CSL and SSPP-modified antenna respectively.

the vertical radiations have been increased at least 3 dBi (figure 2(d)). Since both antennas show $z$-mirror symmetry, the radiations along $\pm z$ directions are the same.

We then disclose that horizontal leakages are produced by the electrode modes. Here, we analyze the dispersion relations and eigenmode distributions by utilizing CST Microwave Studio. The backgrounds are 1600 $\mu$m along the $y$ directions, and 200 $\mu$m along the $z$ directions. The boundary conditions are periodic along the $x$ direction, and perfect electric conductors along the $y$ and $z$ directions. We further show the simulated field patterns of the 3rd and 4th modes on the $x$–$y$ (Figures S1(c) and (d) in SI) and $y$–$z$ planes (Figure S1(g) and (h) in SI) (https://stacks.iop.org/NJP/24/073046/mmedia). Obviously, the dominated components ($E_z$ and $E_y$) are well confined around the SSPP structure. It indicates both the 3rd and 4th modes originate from the SSPP structure, instead of the waveguide modes induced by the boundaries of the background box. However, their dispersions, lying above the light line (shown in figure 3(a)), implies their leaky-wave natures. In figure 3(a), the dispersion of the CSL is a straight line without cutoffs, which supports broadband traveling or leaky TL modes. By integrating the SSPP structures, the modified electrode supports four SSPP modes (shown in figure 3(a)), instead of the leaky TL modes. Interestingly, none SSPP mode is excited by the $y$-polarized dipole in the broad band from 0.93 to 1.5 THz. This band is forbidden for the 1st eigenmode, whose cutoff frequency is 0.93 THz. Although 2nd, 3rd and 4th eigenmodes of SSPP all reside in between 0.93 and 1.5 THz, they cannot be efficiently excited by the dipole source located in the gap. We utilize the excitation efficiency [41] $\eta_i = \int \boldsymbol{E}_{\text{d}}^*(\boldsymbol{x},\boldsymbol{y},\boldsymbol{z}) \cdot \boldsymbol{E}_{\text{ei}}(\boldsymbol{x},\boldsymbol{y},\boldsymbol{z})\text{d}\boldsymbol{x}\,\text{d}\boldsymbol{y}\,\text{d}\boldsymbol{z}$ for explanation, where $i$ represents the $i$th eigenmode, $\boldsymbol{E}_{\text{d}}$ and $\boldsymbol{E}_{\text{ei}}$ represent the normalized excitation field of the dipole and the $i$th normalized eigenmode field of the SSPP structure, respectively. Along the $y$ direction, the 2nd eigenmode shown in figure 3(b) exhibits even parity, orthogonal to the mode of the dipole source with $y$-odd parity. Similarly, both excitation efficiencies of 3rd and 4th eigenmodes are vanished, since their odd parities along

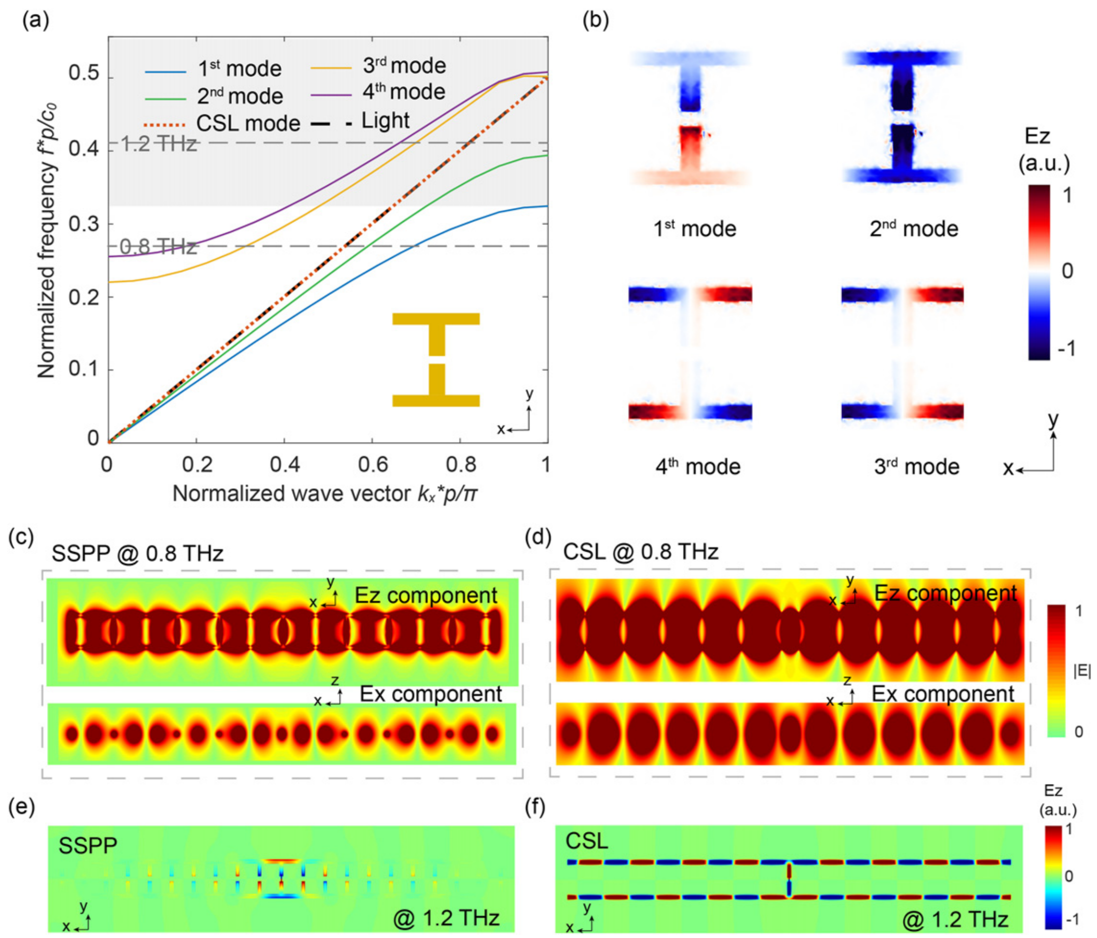


**Figure 3.** The principle of suppressing the electrode modes in SSPP-modified PCAs. (a) The simulated dispersion relations of the CSL (red dotted line), light line (black dotted) SSPP structure (solid lines). The inset shows the unit cell. The dashed line denotes corresponding eigenmodes at 1.0 THz. (b) $E_z$ components for 1st, 2nd, 3rd, and 4th eigenmodes respectively. (c) and (d) The field amplitude excited in the SSPP-modified (c) and the CSL (d) antennas at 0.8 THz. (e) and (f) The $E_z$ components excited in the SSPP-modified (e) and the CSL (f) antennas at 1.2 THz.

the $x$ direction are incompatible with the $x$-even parity of the dipole source. Compared with the near-field patterns of CSL at 0.8 THz (as shown in figure 3(d)), the SSPP mode propagates along the $x$ direction and the fields are confined along both the $y$ and $z$ directions (as shown in figure 3(c)). The excited near-field patterns at 1.2 THz (as shown in figures 3(e)–(f)) further demonstrate the results of suppressing SSPP electrode modes. From the symmetries of the excited SSPP mode shown in figure 3(e), we can tell that the mode pattern at 1.2 THz only belongs to 1st eigenmode, whose propagation is forbidden along the $x$ direction. It is because that 1.2 THz falls into the band gap of 1st eigenmode. In contrast, the TL modes can propagate along the CSL (figure 3(f)), and induce horizontal leakages.

The theoretical analysis above can also be applied in the practical PCA integrated with substrates. We model the GaAs substrate as a 473.7 $\mu$m-thick slab with the relative permittivity $\varepsilon_{\mathrm{GaAs}} = 12.94$. A silicon lens ($\varepsilon_{\mathrm{Si}} = 11.9$) is also integrated for increasing the directivity of PCAs and modeled as a semi sphere with the radius of 1160 $\mu$m, whose focus is set at the location of dipole sources. Both metallic structures remain the same as above. Integrating with the substrate and lens, the SSPP-modified antenna still shows about 2 dBi higher directivity (in figure 4(a)) than that of the CSL. Due to the high permittivity of the substrate, the operational bandwidth is downshifted to the frequency range from 0.35 to 0.57 THz, which is consistent with the cutoff frequency of 1st eigenmode as depicted in the inset of figure 4(a). In contrast to the freestanding antennas, the radiation pattern (as shown in figure 4(b)) of substrate-integrated SSPP antenna does not show remarkable suppression of the horizontal leakages. The phenomenon of the similar horizontal leakages is because that the leaky TL modes in CSL are not allowed to radiate into ambient efficiently, rather than the disfunction of SSPP structures. The low outcoupling of TL modes is accounted to the impedance mismatching between the air and the high-permittivity substrate, which highly confines the THz waves. The substrate confinement is also verified with the drastic reduction of $-z$-direction radiation.

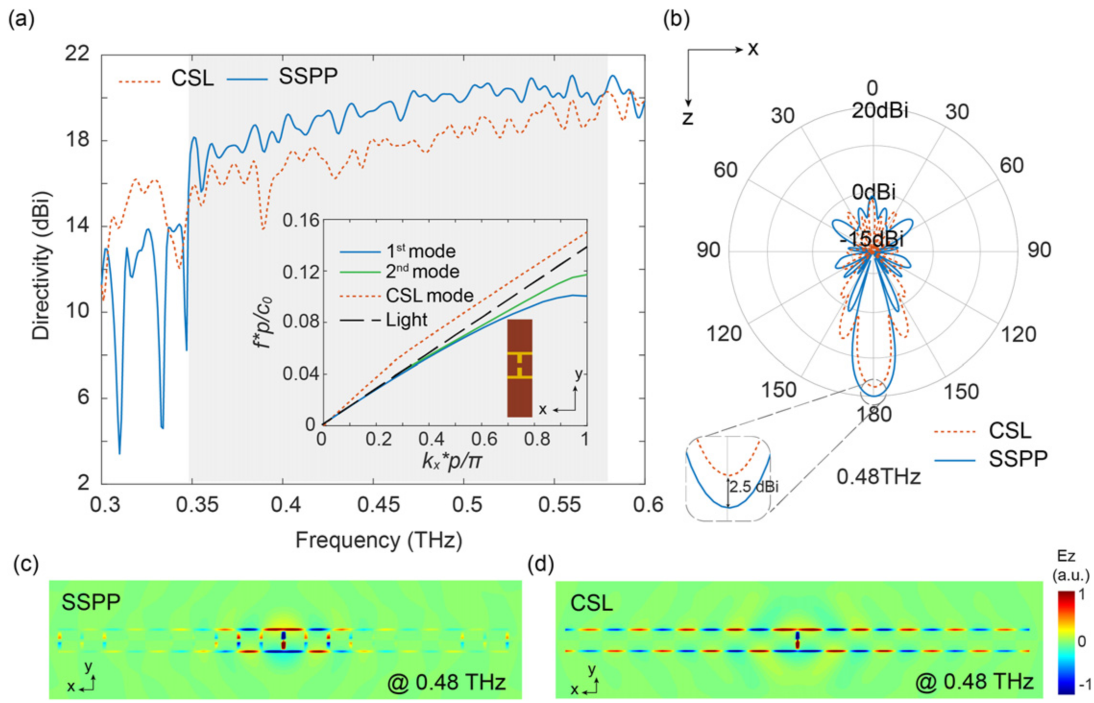


**Figure 4.** The directivity of substrate-integrated SSPP-modified antenna with silicon lens. (a) The directivities of substrate-integrated CSL (red dashed line) and SSPP (blue solid line) antennas with silicon lens. The inset shows both the dispersion relations of the substrate-integrated CSL, the light line, the 1st and 2nd eigenmodes of substrate-integrated SSPP structure, whose corresponding unit cell is also shown in the inset. (b) The radiation patterns in $x$–$z$ plane of both antennas at 0.48 THz. (c) and (d) The near-field patterns excited at 0.48 THz in the substrate-integrated SSPP (c) and the substrate-integrated CSL antennas (d), respectively.

The near-field patterns in figures 4(c) and (d) show that the substrate-integrated SSPP structures can still suppress the horizontal SSPP electrode modes, consistent with above freestanding case.

For further demonstrating the performance of SSPP-PCA, we replace the excitation of dipole source with the practical photo-generated current. The optical-to-THz conversion process consists of two steps, including photocurrent generation excited by a femtosecond optical pulse, and terahertz generation from the PCA. We numerically studied the two steps with COMSOL Multiphysics and CST respectively, where Maxwell's equations and drift-diffusion model are solved simultaneously. Regarding the first step, the optical pulse penetrating the GaAs, generates carriers, and then the electric field strength ($E = 1.33$ V $\mu$m$^{-1}$) drives the carriers to drift along the $y$ direction, thus forming the photocurrent. We numerically study this process with a two-dimensional model, whose simulation area is 10 $\mu$m $\times$ 25 $\mu$m on the $y$–$z$ cross-section. The femtosecond optical pulse follows the Gaussian shape, whose temporal center and width are 2 ps and 133 fs respectively. The optical pulses also have a spatial Gaussian distribution along the $y$ direction, whose half-power beam width is 2 $\mu$m. Taking the center wavelength $\lambda = 800$ nm of the pulse, we show its optical field spatial distribution on the GaAs substrate in figure 5(a). Driven by the electric field strength $E = 1.33$ V $\mu$m$^{-1}$, the photo-generated carriers form transient photocurrent $I_{\mathrm{comsol}}(t)$ as depicted in figure 5(b), which quickly decays in several picoseconds. Taking the peak photocurrent at 2 ps, we show the electron spatial concentration in figure 5(c), which is consistent with the field distribution in figure 5(a). To numerically study the second step, we decompose the obtained transient current into Fourier components, whose coefficients are $A(f) = \int I_{\mathrm{comsol}}(t)\mathrm{e}^{-\mathrm{i}2\pi ft}\,\mathrm{d}t$. The spectral response of the SSPP-PCA that is a 3D geometry is simulated in CST. The output radiation power $P_{\mathrm{THz}}(f)$ is shown in figure 5(d), which is proportional to the input current $I(f)$. Compared with the typical PCA, the radiation power of the SSPP-modified PCA increases around 2 dB in the band 0.45–0.62 THz. We further obtain the total output radiation power with $\int A(f)P_{\mathrm{THz}}(f)\mathrm{d}f$. The optical-to-THz conversion efficiencies of the SSPP-modified PCAs are estimated to be $8.26 \times 10^{-5}$.

The major parameters of optical and electrical properties in the simulation are shown in table 1 (the other details in SI section E).

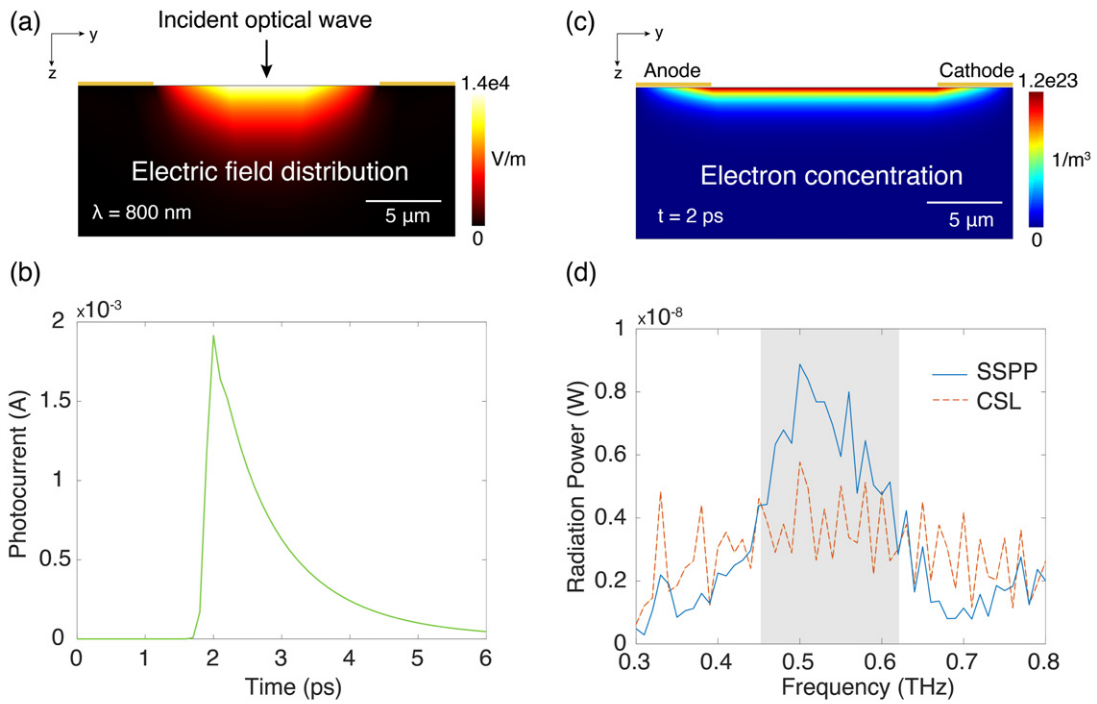


**Figure 5.** The process of optical-to-THz conversion. (a) The electric field distribution of the cross-section in GaAs substrate due to an incident optical wave ($\lambda = 800$ nm). (b) The induced photocurrent in response to an optical pump pulse. (c) The electron concentration on the cross section of the substrate at 2 ps. (d) The comparison of the radiation power between the SSPP-modified PCA and the typical PCA.

**Table 1.** Optical and electrical properties.

| Symbol | Description | Unit | Value |
|---|---|---|---|
| $\lambda$ | Free-space wavelength | nm | 800 |
| $P$ | Incident power | $\mu$W | 10 |
| $t_0$ | Pulse center location | ps | 3 |
| $D_y$ | Pulse HPBW | $\mu$m | 2 |
| $D_t$ | Pulse FWHM | fs | 133 |
| $E$ | The electric field strength | V $\mu$m$^{-1}$ | 1.33 |
| $\varepsilon_{GaAs}$ | GaAs | None | 12.94 |
| $k_{PC}$ | Photoconductor extinction coefficient of GaAs | None | 0.0625 |

## 3. Conclusion

In summary, we propose a SSPP-modified electrode for increasing the directivity of THz PCAs. The underlying principle is suppressing the horizontal SSPP electrode modes. Compared with the conventional CSL PCA, we numerically demonstrate that the directivity of SSPP-modified one is increased around 2 dBi. Since the SSPP-modified electrode is planar, it is compatible the well-developed micro fabrication technologies. Meanwhile, the microscale SSPP structure could be combined with the nanoscale metamaterial structures [9–22] which may increase photocarrier concentration for further increasing the THz output power. Our proposal could enable rich applications in high-performance terahertz sources.

## Acknowledgments

This work was supported by National Natural Science Foundation of China (NNSFC) under Grants No. 62171406, 61801426, No.11961141010, ZJNSF under Grant No. Z20F010018, National Key Laboratory Foundation No. 6142205200402, and the Fundamental Research Funds for the Central Universities No. 2020XZZX002-15.

## Conflict of interest

The authors declare no competing interests.

## Data availability

The data that support the findings of this study are available from the corresponding author upon reasonable request.

## ORCID iDs

Hongsheng Chen https://orcid.org/0000-0002-5735-9781
Wei E I Sha https://orcid.org/0000-0002-7431-8121
Fei Gao https://orcid.org/0000-0001-9928-9390

## References

[1] Auston D H, Cheung K P and Smith P R 1984 Picosecond photoconducting Hertzian dipoles *Appl. Phys. Lett.* **45** 284–6
[2] Ketchen M B, Grischkowsky D, Chen T C, Chi C C, Duling I N, Halas N J, Halbout J M, Kash J A and Li G P 1986 Generation of subpicosecond electrical pulses on coplanar transmission lines *Appl. Phys. Lett.* **48** 751–3
[3] Nagatsuma T, Ducournau G and Renaud C C 2016 Advances in terahertz communications accelerated by photonics *Nat. Photon.* **10** 371–9
[4] Sarieddeen H, Saeed N, Al-Naffouri T Y and Alouini M-S 2020 Next generation terahertz communications: a rendezvous of sensing, imaging, and localization *IEEE Commun. Mag.* **58** 69–75
[5] Mittleman D M 2018 Twenty years of terahertz imaging [invited] *Opt. Express* **26** 9417–31
[6] Kawase K, Ogawa Y, Watanabe Y and Inoue H 2003 Non-destructive terahertz imaging of illicit drugs using spectral fingerprints *Opt. Express* **11** 2549–54
[7] Meijer A S, Berden G, Arslanov D D, Ozerov M, Jongma R T and van der Zande W J 2016 An ultrawide-bandwidth single-sideband modulator for terahertz frequencies *Nat. Photon.* **10** 740–4
[8] Lu X, Venkatesh S and Saeidi H 2021 A review on applications of integrated terahertz systems *China Commun.* **18** 175–201 terahertz wireless communications
[9] Gregory I S, Baker C, Tribe W R, Bradley I V, Evans M J, Linfield E H, Davies A G and Missous M 2005 Optimization of photomixers and antennas for continuous-wave terahertz emission *IEEE J. Quantum Electron.* **41** 717–28
[10] Liu S, Shou X and Nahata A 2011 Coherent detection of multiband terahertz radiation using a surface plasmon-polariton based photoconductive antenna *IEEE Trans. THz Sci. Technol.* **1** 412–5
[11] Park S-G, Jin K H, Yi M, Ye J C, Ahn J and Jeong K-H 2012 Enhancement of terahertz pulse emission by optical nanoantenna *ACS Nano* **6** 2026–31
[12] Heshmat B, Pahlevaninezhad H, Pang Y, Masnadi-Shirazi M, Burton Lewis R, Tiedje T, Gordon R and Darcie T E 2012 Nanoplasmonic terahertz photoconductive switch on GaAs *Nano Lett.* **12** 6255–9
[13] Park S-G, Choi Y, Oh Y-J and Jeong K-H 2012 Terahertz photoconductive antenna with metal nanoislands *Opt. Express* **20** 25530
[14] Berry C W, Wang N, Hashemi M R, Unlu M and Jarrahi M 2013 Significant performance enhancement in photoconductive terahertz optoelectronics by incorporating plasmonic contact electrodes *Nat. Commun.* **4** 1622
[15] Jooshesh A, Smith L, Masnadi-Shirazi M, Bahrami-Yekta V, Tiedje T, Darcie T E and Gordon R 2014 Nanoplasmonics enhanced terahertz sources *Opt. Express* **22** 27992–8001
[16] Burford N M, Evans M J and El-Shenawee M O 2018 Plasmonic nanodisk thin-film terahertz photoconductive antenna *IEEE Trans. THz Sci. Technol.* **8** 237–47
[17] Lepeshov S, Gorodetsky A, Krasnok A, Rafailov E and Belov P 2017 Enhancement of terahertz photoconductive antenna operation by optical nanoantennas *Laser Photon. Rev.* **11** 1770001
[18] Mitrofanov O, Siday T, Thompson R J, Luk T S, Brener I and Reno J L 2018 Efficient photoconductive terahertz detector with all-dielectric optical metasurface *APL Photon.* **3** 051703
[19] Rana G, Bhattacharya A, Gupta A, Ghindani D, Jain R, Duttagupta S P and Prabhu S S 2019 A polarization-resolved study of nanopatterned photoconductive antenna for enhanced terahertz emission *IEEE Trans. THz Sci. Technol.* **9** 193–9
[20] Siday T, Vabishchevich P P, Hale L, Harris C T, Luk T S, Reno J L, Brener I and Mitrofanov O 2019 Terahertz detection with perfectly-absorbing photoconductive metasurface *Nano Lett.* **19** 2888–96
[21] Wang K, Gu J, Shi W, An Y, Li Y, Tian Z, Ouyang C, Han J and Zhang W 2020 All-dielectric nanograting for increasing terahertz radiation power of photoconductive antennas *Opt. Express* **28** 19144–51
[22] Wang N, Cakmakyapan S, Lin Y-J, Javadi H and Jarrahi M 2019 Room-temperature heterodyne terahertz detection with quantum-level sensitivity *Nat. Astron.* **3** 977–82
[23] Lavrukhin D V *et al* 2019 Terahertz photoconductive emitter with dielectric-embedded high-aspect-ratio plasmonic grating for operation with low-power optical pumps *AIP Adv.* **9** 015112
[24] Ponomarev D S *et al* 2019 Enhanced terahertz emission from strain-induced InGaAs/InAlAs superlattices *J. Appl. Phys.* **125** 151605
[25] Singh A, Welsch M, Winnerl S, Helm M and Schneider H 2019 Improved electrode design for interdigitated large-area photoconductive terahertz emitters *Opt. Express* **27** 13108–15
[26] Kohlhaas R B, Breuer S, Liebermeister L, Nellen S, Deumer M, Schell M, Semtsiv M P, Masselink W T and Globisch B 2020 637 $\mu$W emitted terahertz power from photoconductive antennas based on rhodium doped InGaAs *Appl. Phys. Lett.* **117** 161114
[27] Takano K, Chiyoda Y, Nishida T, Miyamaru F, Kawabata T, Sasaki H, Takeda M W and Hangyo M 2011 Optical switching of terahertz radiation from meta-atom-loaded photoconductive antennas *Appl. Phys. Lett.* **99** 161114

[28] O'Hara J F, Chen H-T and Taylor A J 2007 Split-ring resonator enhanced terahertz antenna *Nonlinear Optics: Materials, Fundamentals and Applications TuB2* (Optical Society of America)
[29] Salamin Y, Benea-Chelmus I-C, Fedoryshyn Y, Heni W, Elder D L, Dalton L R, Faist J and Leuthold J 2019 Compact and ultra-efficient broadband plasmonic terahertz field detector *Nat. Commun.* **10** 5550
[30] Shi X, Wang K, Gu J, An Y, Jia R, Tian Z, Ouyang C, Han J and Zhang W 2020 Photoconductive meta-antenna enabling terahertz amplitude spectrum manipulation *Adv. Photon. Res.* **2** 2000036
[31] Lee K, Lee S C, Kim W T, Park J, Min B and Rotermund F 2020 Terahertz generation by a resonant photoconductive antenna *Curr. Optics Photon.* **4** 373–9
[32] Deng H, Xiong Z, Qu W, Wu Z, Liu Q, Chen L, Guo J and Shang L 2020 The impact of structural parameters of split-ring resonators on the terahertz radiation characteristics of micro-structured photoconductive antennas: a simulation study *IEEE Photon. J.* **12** 1–13
[33] Shen X, Cui T J, Martin-Cano D and Garcia-Vidal F J 2013 Conformal surface plasmons propagating on ultrathin and flexible films *Proc. Natl. Acad. Sci. USA* **110** 40–5
[34] Woolf D, Kats M A and Capasso F 2014 Spoof surface plasmon waveguide forces *Opt. Lett.* **39** 517–20
[35] Garcia-Vidal F J, Fernández-Domínguez A I, Martin-Moreno L, Zhang H C, Tang W, Peng R and Cui T J 2022 Spoof surface plasmon photonics *Rev. Mod. Phys.* **94** 025004
[36] Gao F, Gao Z, Luo Y and Zhang B 2016 Invisibility dips of near-field energy transport in a spoof plasmonic metadimer *Adv. Funct. Mater.* **26** 8307–12
[37] Gao Z, Gao F, Zhang Y, Xu H, Luo Y and Zhang B 2017 Forward/Backward switching of plasmonic wave propagation using sign-reversal coupling *Adv. Mater.* **29** 1700018
[38] Gao Z, Wu L, Gao F, Luo Y and Zhang B 2018 Spoof plasmonics: from metamaterial concept to topological description *Adv. Mater.* **30** e1706683
[39] Duffy S M, Verghese S, McIntosh A, Jackson A, Gossard A C and Matsuura S 2001 Accurate modeling of dual dipole and slot elements used with photomixers for coherent terahertz output power *IEEE Trans. Microwave Theory Tech.* **49** 1032–8
[40] Pozar D M 2011 *Microwave Engineering* 4th edn (New York: Wiley)
[41] Joannopoulos J D, Johnson S G, Winn J N and Meade R D 2008 *Photonic Crystals: Modeling the Flow of Light* (Princeton, NJ: Princeton University Press) ch 1